Unified Theory of Thermal Quenching in Inorganic Phosphors

Mahdi Amachraa[a†], Zhenbin Wang[b†], Hanmei Tang[a], Shruti Hariyani[c], Chi Chen[b], Jakoah Brgoch[c], Shyue Ping Ong[b*]

[a]Materials Science and Engineering Program, University of California San Diego, 9500 Gilman Dr, Mail Code 0418, La Jolla, CA 92093-0448, United States

[b]Department of NanoEngineering, University of California San Diego, 9500 Gilman Dr, Mail Code 0448, La Jolla, CA 92093-0448, United States

[c]Department of Chemistry, University of Houston, College of Natural Sciences and Mathematics, Science & Research Building 1, 3507 Cullen Blvd, Room 214, Houston, Texas 77204-5008

[†]These authors contributed equally to this work.

E-mail: ongsp@eng.ucsd.edu

Abstract

We unify two prevailing theories of thermal quenching (TQ) in rare-earth-activated inorganic phosphors – the cross-over and auto-ionization mechanisms – into a single predictive model. Crucially, we have developed computable descriptors for activator environment stability from *ab initio* molecular dynamics simulations to predict TQ under the cross-over mechanism, which can be augmented by a band gap calculation to account for auto-ionization. The resulting TQ model predicts the experimental TQ in 29 known phosphors to within ~ 10-11%. Finally, we have developed an efficient topological approach to rapidly screen vast chemical spaces for the discovery of novel, thermally robust phosphors.

Main Manuscript

Lighting accounts for approximately 15% of global energy consumption and 5% of CO_2 emission.[1] Solid-state lighting (SSL) based on phosphor-converted light-emitting diodes (pc-LEDs) is ~ 10x more efficient than traditional lighting and therefore offers a huge opportunity to achieve substantial energy savings and CO_2 reductions. A critical component in pc-LEDs are the rare-earth substituted inorganic phosphors, which down-convert the near-ultraviolet or blue LED emission to longer wavelengths and generate white light. The phosphors currently employed in these bulbs are comprised of an inorganic host material, like an oxide or nitride that has been substituted with a rare-earth ion that is typically Ce^{3+} or Eu^{2+}. The prototypical phosphor used in a majority of lighting devices is yttrium aluminum garnet, $Y_3Al_5O_{12}$ or YAG, substituted with Ce^{3+} to produce a bright yellow emission. Exciting this phosphor when it is coated on top of a blue LED chip produces a mixture of blue and yellow emissive lights that combine and appears white to the eye.

Developing phosphors with high quantum efficiency and excellent thermal stability is a long-standing quest within the SSL community. There has been some progress in the development of methods to understand phosphor efficiency, but thermal stability remains a major challenge. The emission loss with increasing temperature (also known as thermal quenching or TQ) is of particular importance to next-generation SSL, where high-power LEDs and laser-based LEDs are becoming more common, which in combination with smaller device packaging, generates more heat that can negatively influence the optical output. The TQ of a phosphor is experimentally determined by taking the ratio of integrated light intensity emitted at operating temperature, which is generally considered ~ 150 – 200 ℃ and the integrated intensity of light emitted at room temperature. Commercial phosphors, such as YAG:Ce^{3+}, have TQ of less than 10%, meaning only

a majority of the emission intensity is maintained at high temperature, whereas other phosphors can be completely thermally quenched (TQ = 100%) at high temperature. It is therefore unsurprising that extensive efforts have been devoted to the investigation of the TQ mechanism in phosphors. [2–5]

Two dominant theories have been proposed to explain the TQ behavior in Ce^{3+} and Eu^{2+}-activated phosphors. In the 1960s, Blasse *et al.* proposed that TQ is the result of the non-radiative relaxation of electrons from the excited state to the ground state. [6,7] This "cross-over" mechanism is represented schematically using the configuration coordinate diagram in Fig. 1, where the energy difference between the excited state and the cross-over point (E_a^{co}) determines the activation barrier for this process. This theory forms the base of searching for structurally rigid phosphor hosts, as indicated by a high Debye temperature (Θ_D), as a proxy of low TQ. [3] The fundamental assumption here is that the more rigid the host, the more unlikely non-radiative relaxation from the excited configuration to the ground state configuration occurs. However, subsequent experiments have found many violations of this relationship; for example, the $Ca_7Mg(SiO_4)_4$:Eu^{2+}, $CaMgSi_2O_6$:Eu^{2+}, and $Sr_6M_2Al_4O_{15}$:Eu^{2+} (M = Y, Lu, Sc) phosphors all suffer from thermal quenching despite their high Debye temperatures. [8,9] The second theory of TQ is attributed to Dorenbos. In the Dorenbos model, TQ is due to the thermal excitation of the excited 5*d* electron of Ce^{3+}/Eu^{2+} to the conduction band of the host; [5] the activation barrier of this auto-ionization process (E_a^{ai} in Fig. 1) determines the TQ of a phosphor, and this barrier is in turn correlated to the band gap of the phosphor host. [10] There are other TQ pathways as well, although these two competing mechanisms are the primary drivers in the of loss luminescence as a function of temperature.

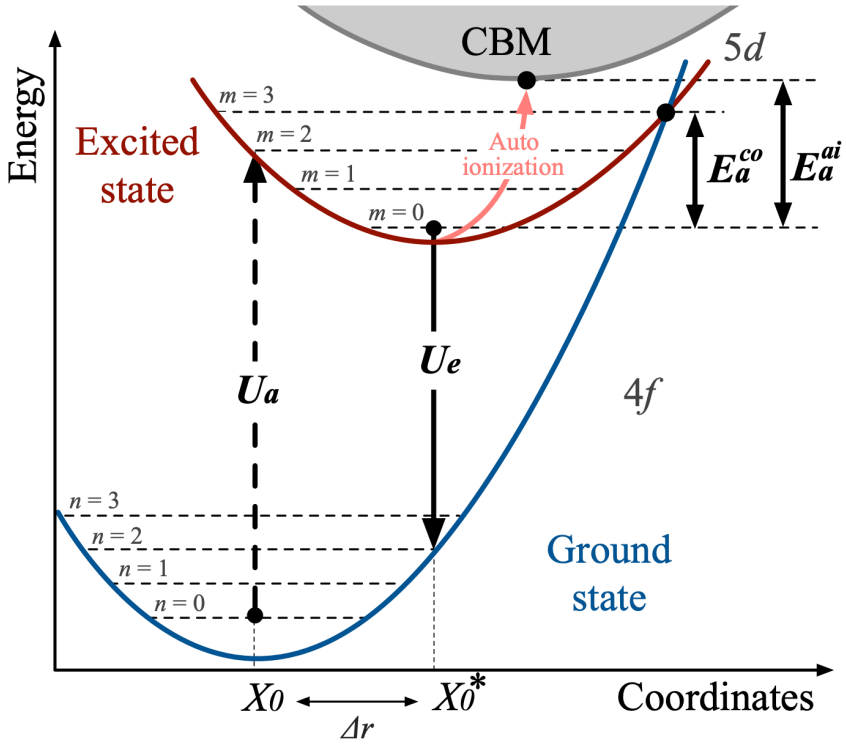

FIG. 1. Configurational coordinate diagram for the activator in a phosphor. Excitation is allowed from the vibrational level $n = 0$ of the ground states to the excited state and results in the absorption energy U_a. The relaxation of the system from the vibrational level $m = 0$ to the ground state results in the emission energy U_e. The displacement $\Delta r = X_0^* - X_0$ is the polyhedron average bond length difference between the excited and ground state of the activator. In the cross-over model, thermal quenching results from the non-radiative relaxation of an excited electron to the ground state when the temperature is high enough to overcome the activation energy E_a^{co}. In the Dorenbos auto-ionization model, thermal quenching results from the promotion of excited electrons to the conduction band minimum if the temperature is high enough to overcome the activation energy E_a^{ai}.

In this letter, we develop a unified theory of TQ in phosphors by considering the competition between the two prevailing TQ mechanisms. The focus of this work is specifically on TQ in Ce^{3+} and Eu^{2+}-activated phosphors, which are the most common rare-earth ions employed in phosphors and operate on the highly efficient $4f^n5d^0 \rightarrow 4f^{n-1}5d^1$ transition. Using *ab initio* molecular dynamics simulations, we establish that the local environment stability around the rare-earth ion as a function of temperature is a robust, transferable descriptor for TQ under the cross-over mechanism when the host band gap is sufficiently large. If the phosphor host's band gap is

small, however, the auto-ionization mechanism competes with the cross-over mechanism. We therefore develop a model accounting for both quenching mechanisms to predict TQ of the phosphors. For this analysis, a total of 29 oxide phosphors with experimentally-measured TQ values were selected to construct the models. Information on these phosphors is summarized in Table SI. It should be noted that nitride and oxynitride phosphors are excluded from this work due to substantial differences in bonding. Our results show that the combination of AIMD simulations and band gap calculations provide a clear relationship between a series of computed descriptors and the thermal quenching at high temperature. Furthermore, we propose a novel topological descriptor based on the Voronoi analysis that can be used to rapidly screen for low TQ phosphors without expensive AIMD simulations, thereby allowing the discovery of new thermally robust inorganic phosphors.

Ab initio molecular dynamics (AIMD) simulations were performed on the 29 phosphors at room temperature (300 K) as the initial temperature and 500 K as the final reference temperature. [11] All calculations were performed using the Perdew-Burke-Ernzerhof (PBE) functional [12] with a Hubbard *U* value of 2.5 eV [13,14] for the 4*f* orbitals Eu^{2+} and Ce^{3+} (see Methods in SI for details). For each phosphor, an activator environment distribution (AED) at both temperatures was constructed from the AIMD trajectories. The AED is derived by determining the number of simulation timesteps that the activator has a particular coordination number (CN) using the algorithm developed by Waroquiers et al., [15] normalized across the total number of timesteps. Fig. 2 presents the AED for three Ce^{3+} and three Eu^{2+}-activated phosphors with high (> 80%), intermediate (40-60%) and low (< 20%) TQ. Similar plots for the remaining 23 phosphors are provided in Fig. S1 and S2. Comparing the AEDs between 300 K and 500 K, we observe that small TQ (*i.e.*, thermally robust) phosphors have minimal changes in the AED whereas the high

TQ (*i.e.*, thermally quenched) phosphors show substantial shifts in the AED. For example, the Ce^{3+} in YAG:Ce^{3+} (TQ = 6%) is primarily eight-fold coordinated with oxygen and its CN remains stable at 500 K. In contrast, the Ce^{3+} in $Ba_2Y_5B_5O_{17}$:Ce^{3+} (TQ = 71%) has a distribution of CN of 7-8 at 300 K and exhibits an obvious shift to lower CNs, including seven-fold and six-fold coordination environments, at 500 K. The same trend is observed for Eu^{2+}-activated phosphors in Fig. 2(b).

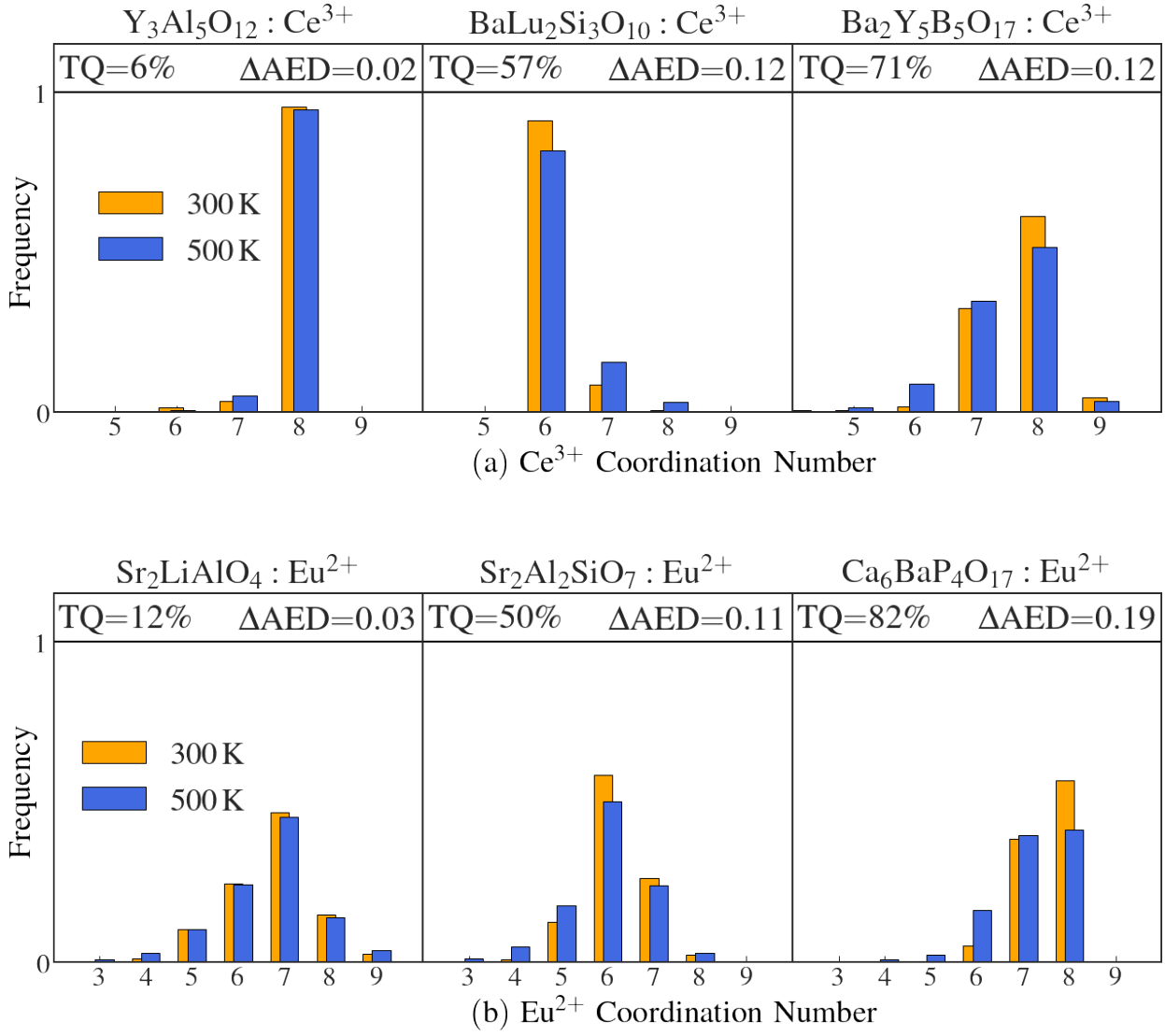

FIG. 2. Activator environment distribution (AED). The computed AED of (a) Ce^{3+} and (b) Eu^{2+} at 300 K and 500 K in three hosts with distinct TQ behaviors. The experimental TQ values were obtained from references [11–17].

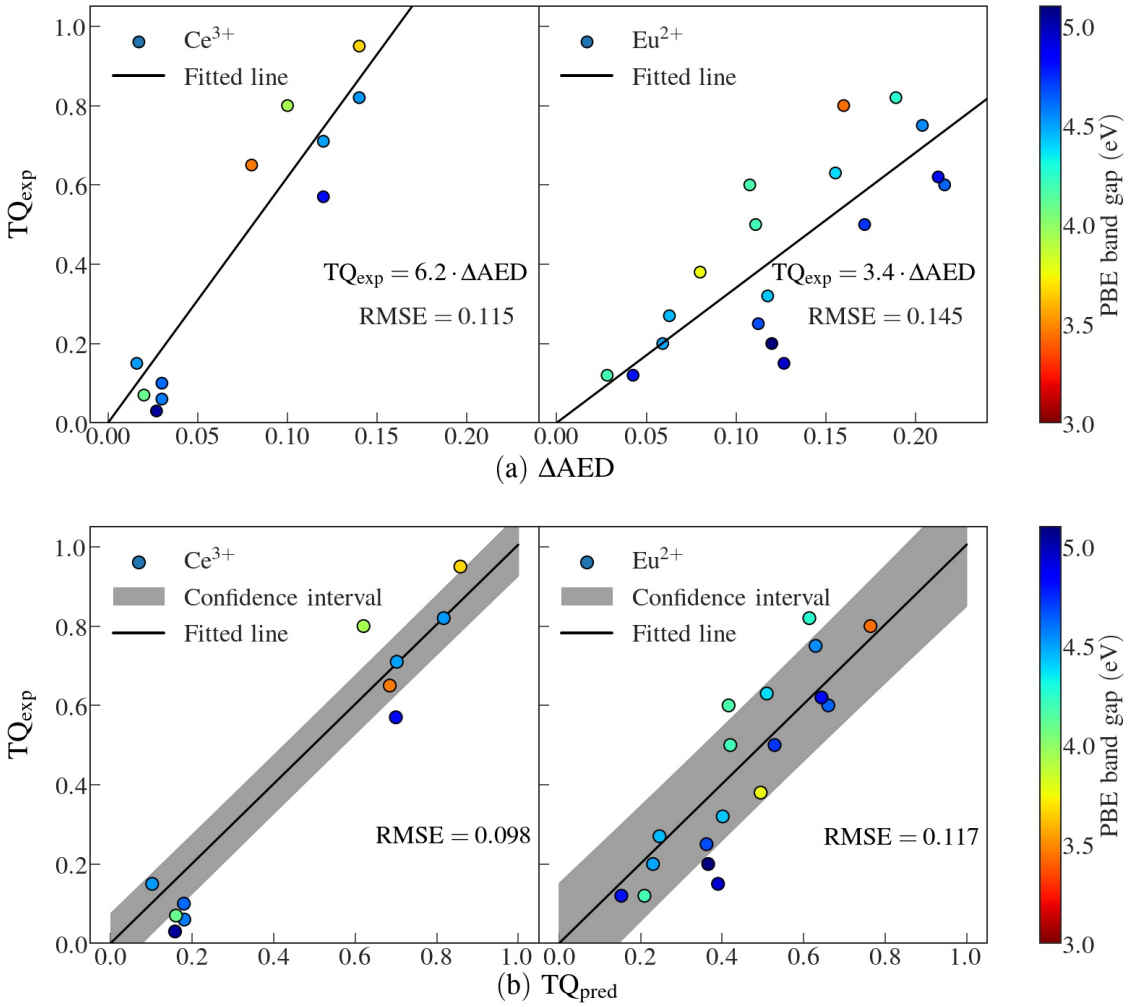

FIG. 3. Models for TQ. (a) Plot of experimental thermal quenching (TQ_{exp}) against the change in the activator environment distribution (ΔAED) for Ce^{3+} (left) and Eu^{2+} (right) activated phosphors. (b) Plot of TQ_{exp} against the predicted TQ (TQ_{pred}) from the unified TQ model [Eq. (2)] for Ce^{3+} (left) and Eu^{2+} (right)-activated hosts. The marker colors are based on their calculated band gap using the Perdew-Burke-Ernzerhof (PBE) functional (see color bar). The root mean square error (RMSE) for each model is defined as the square root of the average squared difference between the predicted TQ (TQ_{pred}) and the experimental TQ (TQ_{exp}), i.e. $\mathrm{RMSE} = \sqrt{\frac{1}{N}\sum_{i=1}^{N}\left(\mathrm{TQ}^{\mathrm{i}}_{\mathrm{pred}} - \mathrm{TQ}^{i}_{exp}\right)^2}$.

TABLE I. Optimized coefficients from non-linear least-squared minimization of unified TQ model for Ce^{3+} and Eu^{2+} activated hosts.

	A	*B*	*K*
Ce^{3+}	0.17	0.039 eV	5.83
Eu^{2+}	0.12	0.33 eV	2.98

To quantify the shift in the AED from 300 K to 500 K, we define ΔAED as the Euclidean distance between AEDs at 300 K and 500 K as follows:

$$\Delta\text{AED} = \sqrt{\sum_{x=2}^{12}(\omega_{CN=x}^{300K} - \omega_{CN=x}^{500K})^2} \quad (1)$$

where, $\omega_{CN=x}^{300K}$ and $\omega_{CN=x}^{500K}$ are the normalized CN frequencies at 300 K and 500 K, respectively, and the CN ranges from 2 to 12. Fig. 3(a) shows the experimental TQ (TQ_{exp}) against the computed ΔAED for Ce^{3+} and Eu^{2+}-activated phosphors. We find there is a clear positive correlation between TQ and ΔAED for both Ce^{3+} and Eu^{2+}-activated phosphors. A least-squares fitting for the one-parameter expression $TQ = K\Delta AED$, where K is a constant, yields R^2 values of 0.89 and 0.62 for Ce^{3+} and Eu^{2+}-activated phosphors, respectively, with reasonable root mean square errors (RMSEs) of 11.5% and 14.5%, respectively. In contrast, the DFT-calculated Debye temperature (Θ_D) yields a much weaker correlation against TQ_{exp} (see Fig. S3) with R^2 values of 0.14 and 0.12 for Ce^{3+} and Eu^{2+}-activated phosphors, respectively, with corresponding RMSEs of 32% and 26%, respectively. While there is some correlation between ΔAED and host structural rigidity, as suggested by the high Debye temperatures, coordinated local displacements within a crystal environment are more directly related to the low ΔAEDs, making it more reliable compared to a global descriptor like structural rigidity. These observations support our hypothesis that ΔAED is an excellent descriptor to probe the depth of the potential energy surface (PES) in the cross-over model, where a higher ΔAED implies a shallower PES in the ground and excited states, which results in a lower E_a^{co} and higher TQ.

Close examination of Fig. 3(a) further reveals that phosphors with large host band gaps (E_g) lie below the regression line, and those with small E_g lie above the line. This observation

suggests that E_g, which is a proxy descriptor for TQ under the Dorenbos auto-ionization model, also plays a critical role in modeling TQ for some materials. Considering the cross-over model and the auto-ionization model for quenching are two independent sources of TQ, it is likely both are occurring simultaneously in some phosphor systems. Therefore, we combine ΔAED with the Dorenbos expression for TQ [5] under the auto-ionization model (detailed derivations are provided in Supplemental Materials) to derive a new formula of $\mathrm{TQ_{pred}}$ as follows:

$$\mathrm{TQ} = 1 - (1 - K\Delta\mathrm{AED})\frac{1 + C \cdot e^{\frac{-E_a^{ai}}{k_B T_1}}}{1 + C \cdot e^{\frac{-E_a^{ai})}{k_B T_2}}} \tag{2}$$

where, k_b is the Boltzmann constant, T_1 (300 K) is the initial temperature in Kelvin, T_2 is the final temperature of quenching, which in these calculations is 500 K, C is defined as the ratio of the attempt rate for thermal quenching (Γ_0) and the radiative decay rate of the 5*d* state (Γ_v), [5,11], and E_a^{ai} is the barrier for auto-ionization under the Dorenbos model. Further, we express the auto-ionization barrier as a linear function of the computed PBE band gap, as follows:

$$E_a^{ai} = AE_g + B \tag{3}$$

where *A* and *B* are fitted constants. This linear fit accounts for the relationship between the auto-ionization barrier and E_g, but also the well-known systematic underestimation of E_g by the PBE functional. The optimal values of *K*, *A* and *B*, were determined by performing a non-linear least-square minimization of the predicted TQ from Eq. (2) with experimentally-observed TQ of the 29 phosphors (see Table SI) and are tabulated in Table I. Ce^{3+} and Eu^{2+}-activated phosphors are expected to have different *A* and *B* values because of their large difference in energy gap between the 4*f* ground state and the 5*d* excited state (6.2 eV and 4.2 eV for free Ce^{3+} and Eu^{2+} ions, respectively). [23] Fig. 3(b) plots the predicted $\mathrm{TQ_{pred}}$ using the optimized Eq. (2) against the

experimental TQ_{exp}. The RMSE for Ce^{3+} and Eu^{2+} are 9.8% and 11.7%, respectively, which are a significant improvement over the model using ΔAED alone. A further validation of our unified TQ model can be seen in the fact that the predicted E_a^{ai} (provided in Table SI) are in good agreement with experimental auto-ionization energies. For example, the predicted E_a^{ai} of $Sr_2MgSi_2O_7:Eu^{2+}$, $Y_3Al_5O_{12}:Ce^{3+}$, and $Lu_3Al_5O_{12}:Ce^{3+}$ are 0.83 eV, 0.81 eV and 0.89 eV, respectively, and the corresponding experimental auto-ionization energies are 0.9 eV, 0.77 eV, and 0.86 eV, respectively. [16,24,25]

The unified TQ equation [Eq. (2)] can be understood intuitively by considering the competition between the cross-over and auto-ionization mechanisms in Fig. 1. The main loss of emission with temperature increase will come from the mechanism with the lowest barrier E_a. When the band gap of the host is large, $E_a^{ai} \gg E_a^{co}$, the cross-over mechanism dominates. ΔAED then describes the potential energy surface and TQ. When the band gap of the host is sufficiently small, both mechanisms compete, and ΔAED and E_g are required to describe TQ.

Finally, we demonstrate how a modified version of the unified TQ model can be used to computationally screen for low TQ phosphors. While the band gap, E_g, can be obtained using relatively inexpensive ground-state DFT computations, ΔAED requires expensive AIMD simulations for activated phosphors, where relatively large supercells of the host crystal are required to simulate the experimental low activator concentration. It is therefore desirable to establish an alternative descriptor for local environment stability. Fig. 4(a) shows a *topological* sensitivity analysis of the local activator environment in $Sr_2SiO_4:Eu^{2+}$ computed using a robust Voronoi tessellation-based algorithm (similar plots for all 29 phosphors are provided in Fig. S4 and S5). [15,26] By varying the distance (α) and angle (γ) parameters, the algorithm yields different coordination environments due to changes in the bond weights of the surrounding ligands

(see Supplemental Materials for bond weights computations). The coordination environment formed by the highest weight ligands determines the main activator local environment, which in $Sr_2SiO_4:Eu^{2+}$ is CN = 6. Our hypothesis is that the larger the normalized area (Υ) occupied by the main activator local environment, the less sensitive the activator local environment is to variations in bond distances and angles. In other words, the higher Υ, the lower the ΔAED and the smaller the expected TQ. Therefore, substituting ΔAED with $1-\Upsilon$ in Eq. (2), we obtain the following alternative model:

$$TQ = 1 - (1 - K'(1-\Upsilon))\frac{1 + C.e^{-\frac{E_a^{ai}}{k_B T_1}}}{1 + C.e^{-\frac{E_a^{ai})}{k_B T_2}}} \quad (4)$$

where *A* and *B* for the E_a^{ai} expression [Eq. (3)] are kept as the optimized values from the non-linear least-squares optimization of Eq. 2, while *K'* is refitted. The optimized values of K' are 0.85 and 0.71 for Ce^{3+} and Eu^{2+}, respectively. Fig. 4(b) plots the TQ_{exp} against TQ'_{pred} as defined by Eq. (4). The RMSE of TQ'_{pred} for Ce^{3+} and Eu^{2+} is 0.324 and 0.137, respectively. While this value of RMSE is higher than the RMSE using Eq. (2), the RMSE using Eq. (4) is already sufficiently low for Eu^{2+}-activated hosts to be used for rapid screening for discovery of low TQ phosphors. The difference in performance between using $(1-\Upsilon)$ and ΔAED, especially for Ce^{3+}-activated hosts, can be attributed to two factors. First, one of the outliers, $Ba_3Y_2B_6O_{15}:Ce^{3+}$ is known to have multiple symmetrically-distinct activator sites, while the Voronoi area was computed using only the most energetically stable site. [19,28] Second, $(1-\Upsilon)$ is a pure topological descriptor with no consideration of differences in chemical bonding whereas ΔAED inherently captures subtle relationships between bond distances, bond angles and bond strength in the distribution of activator

environments. Nevertheless, the ability to quickly obtain ϒ values without computationally expensive AIMD calculations makes this approach ideal for materials screening.

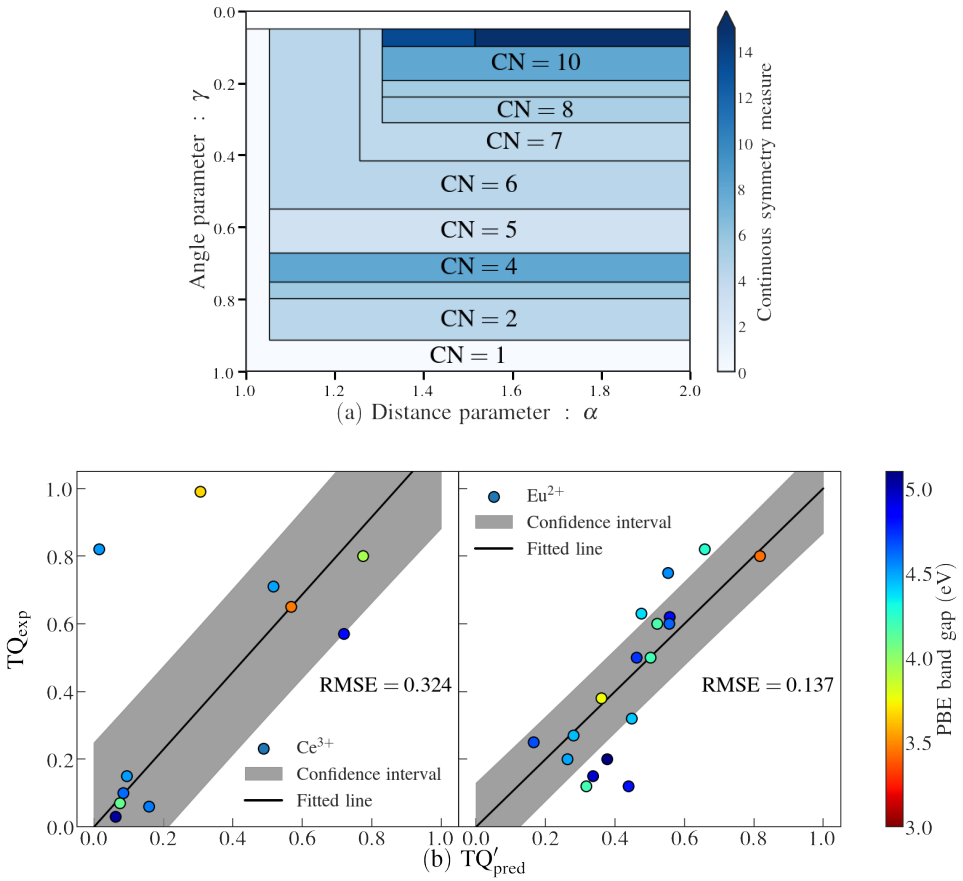

FIG 4. Efficient topological descriptor for TQ. (a) The Voronoi grid representation of Eu^{2+} doped in Sr_2SiO_4. The Voronoi grid representation has two variables: the angle parameter γ and the distance parameter α. For a specific range of angle and distance parameters, a unique coordination number is defined. Each Voronoi grid is representative of a set of ligands denoted by the coordination number. The continuous symmetry measure is used to assess the degree of symmetry within different coordination numbers and developed by Pinsky. [27] (b) Plot of the predicted TQ_{exp} against TQ'_{pred} obtained from modified TQ model utilizing the topological descriptor [Eq. (4)] for Ce^{3+} (left) and Eu^{2+} (right)-activated phosphors.

In summary, we have developed a unified TQ model by integrating the two prevailing theories – the cross-over and auto-ionization models – for thermal quenching in Ce^{3+} and Eu^{2+}-activated phosphors. More critically, we have developed computational approaches to probe thermal quenching in phosphors using this unified TQ model. We establish that local activator

environment stability, as measured by the change in activator environment distribution with temperature in AIMD simulations, ΔAED, is the relevant descriptor for TQ under the cross-over mechanism. The computed host band gap, E_g, is a descriptor for TQ under the auto-ionization mechanism. This unified TQ model combining both ΔAED and E_g predicts the experimentally observed TQ in 29 Ce^{3+} and Eu^{2+}-activated phosphors to within a RMSE of 9.8% and 11.7%, respectively. We have also developed an alternative topological descriptor for local environment stability based on Voronoi tessellation that allows for rapid TQ screening of phosphors without expensive AIMD simulations. This work provides crucial insights into the TQ mechanisms in phosphors and an efficient and reliable way to the discovery of new phosphors with low TQ for next generation, high power solid-state lighting.

Acknowledgements

This work was primarily supported by the National Science Foundation, Ceramics Program, under grant no. 1911372. S. Hariyani and J. Brgoch also acknowledge funding from the National Science Foundation under grant no. 1911311 as well as the Division of Materials Research under grant no. 1847701. The computational resources were provided by the Extreme Science and Engineering Discovering Environment (XSEDE) supported by the National Science Foundation under grant no. ACI-1548562, the Triton Super Computer Center (TSCC) at the University of California, San Diego, and the National Energy Research Scientific Computing Center (NERSC).

*Corresponding author: ongsp@eng.ucsd.edu

References

[1] United Nations Environment Programme, *Accelerating the Global Adoption of Energy-Efficient Lighting - U4E Policy Guide Series* (2017).

[2] S. Poncé, Y. Jia, M. Giantomassi, M. Mikami, and X. Gonze, J. Phys. Chem. C **120**, 4040 (2016).

[3] K. A. Denault, J. Brgoch, S. D. Kloß, M. W. Gaultois, J. Siewenie, K. Page, and R. Seshadri, ACS Appl. Mater. Interfaces **7**, 7264 (2015).

[4] Y. Zhuo, A. Mansouri Tehrani, A. O. Oliynyk, A. C. Duke, and J. Brgoch, Nat. Commun. **9**, (2018).

[5] P. Dorenbos, J. Phys. Condens. Matter **17**, 8103 (2005).

[6] G. Blasse and A. Bril, Phil Tech Rev **31**, 304 (1970).

[7] G. Blasse and B. C. Grabmaier, *Luminescent Materials* (Springer Berlin Heidelberg, Berlin, Heidelberg, 1994).

[8] J. Ha, Z. Wang, E. Novitskaya, G. A. Hirata, O. A. Graeve, S. P. Ong, and J. McKittrick, J. Lumin. **179**, 297 (2016).

[9] A. C. Duke, E. Finley, M. Hermus, and J. Brgoch, Solid State Sci. **60**, 108 (2016).

[10] Z. Wang, I.-H. Chu, F. Zhou, and S. P. Ong, Chem. Mater. **28**, 4024 (2016).

[11] W. Nemitz, P. Fulmek, J. Nicolics, F. Reil, and F. P. Wenzl, Sci. Rep. **7**, (2017).

[12] J. P. Perdew, K. Burke, and M. Ernzerhof, Phys. Rev. Lett. **77**, 3865 (1996).

[13] G. Kresse and J. Furthmüller, Phys. Rev. B **54**, 11169 (1996).

[14] A. Chaudhry, R. Boutchko, S. Chourou, G. Zhang, N. Grønbech-Jensen, and A. Canning, Phys. Rev. B **89**, 155105 (2014).

[15] D. Waroquiers, X. Gonze, G. M. Rignanese, C. Welker-Nieuwoudt, F. Rosowski, M. Göbel, S. Schenk, P. Degelmann, R. André, R. Glaum, and G. Hautier, Chem. Mater. **29**, 8346 (2017).

[16] J. Ueda, P. Dorenbos, A. J. J. Bos, A. Meijerink, and S. Tanabe, J. Phys. Chem. C **119**, 25003 (2015).

[17] K. Li, S. Liang, H. Lian, M. Shang, B. Xing, and J. Lin, J Mater Chem C **4**, 3443 (2016).

[18] M. Hermus, P.-C. Phan, and J. Brgoch, Chem. Mater. **28**, 1121 (2016).

[19] Z. Wang, J. Ha, Y. H. Kim, W. B. Im, J. McKittrick, and S. P. Ong, Joule **2**, 914 (2018).

[20] F.-C. Lu, L.-J. Bai, W. Dang, Z.-P. Yang, and P. Lin, ECS J. Solid State Sci. Technol. **4**, R27 (2014).

[21] W. Zhou, X. Ma, M. Zhang, Y. Luo, and Z. Xia, J. Rare Earths **33**, 700 (2015).

[22] N. Komuro, M. Mikami, Y. Shimomura, E. G. Bithell, and A. K. Cheetham, J. Mater. Chem. C **3**, 204 (2015).

[23] P. Dorenbos, J. Phys. Condens. Matter **15**, 4797 (2003).

[24] A. Chaudhry, R. Boutchko, S. Chourou, G. Zhang, N. Grønbech-Jensen, and A. Canning, Phys. Rev. B - Condens. Matter Mater. Phys. **89**, 155105 (2014).

[25] J. Xu, W. Chen, R. Zeng, and D. Peng, Mater. Lett. **133**, 1 (2014).

[26] S. P. Ong, W. D. Richards, A. Jain, G. Hautier, M. Kocher, S. Cholia, D. Gunter, V. L. Chevrier, K. A. Persson, and G. Ceder, Comput. Mater. Sci. **68**, 314 (2013).

[27] M. Pinsky and D. Avnir, Inorg. Chem. **37**, 5575 (1998).

[28] A. C. Duke, S. Hariyani, and J. Brgoch, Chem. Mater. **30**, 2668 (2018).

Supplemental Material
Unified Theory of Thermal Quenching in Inorganic Phosphors

Mahdi Amachraa[a†], Zhenbin Wang[b†], Hanmei Tang[a], Shruti Hariyani[c], Chi Chen[b], Jakoah Brgoch[c], Shyue Ping Ong[b*]

[a]Materials Science and Engineering Program, University of California San Diego, 9500 Gilman Dr, Mail Code 0418, La Jolla, CA 92093-0448, United States
[b]Department of NanoEngineering, University of California San Diego, 9500 Gilman Dr, Mail Code 0448, La Jolla, CA 92093-0448, United States
[c]Department of Chemistry, University of Houston, College of Natural Sciences and Mathematics, Science & Research Building 1, 3507 Cullen Blvd, Room 214, Houston, Texas 77204-5008
[†]These authors contributed equally to this work.
*Correspondence should be directed to ongsp@eng.ucsd.edu

Methods

Density functional theory (DFT) calculations. All DFT calculations were performed using the Vienna ab initio simulation package (VASP) within the projector-augmented wave method. [1,2] The exchange-correlation interaction was described using the Perdew-Berke-Ernzerhof (PBE) [3] generalized gradient approximation (GGA) functional with the Hubbard U extension to it. In general, the parameters used are similar to those used in the Materials Project [4], with a plane wave energy cutoff of 520 eV and a *k*-point density at least of 100 per $Å^{-3}$. A *U* value of 2.5 eV was used for the 4*f* orbitals in Eu and Ce, as per previous works. [1,5] All structures were fully relaxed with energies and forces converged to within 10^{-5} eV and 0.01 eV/Å, respectively.

To construct the Eu^{2+}/Ce^{3+}-activated phosphors, Eu^{2+}/Ce^{3+} was doped into all compatible symmetrically-distinct sites in supercells of the host crystal with lattice parameters of at least 10 Å in each direction. The lowest energy Eu^{2+}/Ce^{3+}-doped structure was then used for subsequent analysis and AIMD simulations. All crystal structure and data analysis were carried out using the Python Materials Genomics (pymatgen) package. [6]

***Ab initio* molecular dynamics (AIMD).** AIMD simulations were carried out on the supercell models of Eu^{2+}/Ce^{3+}-activated phosphors. The AIMD simulations were in the NVT ensemble at 300 K and 500 K with a Nose-Hoover thermostat [7], and the simulation cell was fixed at the final 0K relaxed cell parameters for each phosphor. To reduce computational cost, the AIMD simulations were non-spin-polarised, and a minimal Γ-centered $1 \times 1 \times 1$ k-point mesh and a time step of 2 fs were adopted.

Debye temperature. The Debye temperatures of all host compounds were calculated using the quasi-harmonic model given by:

$$\Theta = \frac{h}{2\pi k_B}(6\pi^2 V^{\frac{1}{2}} n) f(\nu) \sqrt{\frac{B}{M}}$$

where, V, n, $f(\nu)$, B and M are the unit cell volume, the number of atoms in the unit cell, a scaling function in terms of Poisson's ratio ν, the bulk modulus and the molar mass, respectively; h and k_B refer to the Planck constant, and the Boltzmann constant, respectively. [8]

Activator local environment determination. The activator local environments were computed using the algorithm of Waroquiers *et al.* implemented in pymatgen. [9] Hoppe's effective coordination number (ECoN) was utilized to determine bond weight based on geometry, leading to a chemically guided local environment algorithm. [10] Based on the polyhedron geometry with the highest weight; consequently, a unique cut-off radius or maximum distance factor (MDF) was determined and used to determine the local environment distribution changes during AIMD simulations. The MDF α was computed as follows:

$$\alpha = \frac{l^X}{l^X_{min}},$$

where, l^X, and l^X_{min} are the ligand-activator bond length and the smallest activator-ligand bond length, respectively, and the ECoN values were computed as follows:

$$ECoN = \sum \exp\left(1 - \left(\frac{l_i}{l_{abl}}\right)^6\right), \text{where } l_{abl} = \frac{\sum\left(l_i \exp\left(1 - \left(\frac{l_i}{l_{min}}\right)^6\right)\right)}{\sum\left(\exp\left(1 - \left(\frac{l_i}{l_{min}}\right)^6\right)\right)}$$

l_i, l_{min} and l_{abl} are the ligand-activator bond weight, the lowest ligand-activator bond weight, and the average bond length weight, respectively.

The Voronoi representation computes a polar transformation of an activator's nearest neighbors into a cartesian frame and requires an additional angular parameter:

$$\gamma = \frac{\theta^{\mathrm{x}}}{\theta^{\mathrm{x}}_{\mathrm{max}}}$$

θ^X_{max}, and θ^X are the widest angle to uniquely define a given set of ligands, and the angle at which the local environment is considered.

Derivation of Unified Thermal Quenching Model

The quantum efficiency (QE) of electronic transitions [11] is given by

$$\mathrm{QE}(T) = \frac{1}{1 + C \cdot e^{\frac{-E_a}{k_B T}}} \text{ where } C = \frac{\Gamma_0}{\Gamma_v}$$

where the constant C is defined as the ratio of the attempt rate for thermal quenching (Γ_0) and the radiative decay rate of the 5d state (Γ_v), k_B is Boltzmann's constant, and E_a is the activation energy for the mechanism of loss of emission. C for Eu^{2+} and Ce^{3+} have previously been derived Dorenbos as 2.73×10^7 and 2.3×10^6 respectively. [12,13]

The thermal stability (TS) of a phosphor compound is measured as the ratio of the QE between a lower temperature T_1 and a higher temperature T_2, as follows:

$$\mathrm{TS} = \frac{\mathrm{QE}(T_2)}{\mathrm{QE}(T_1)} = \frac{1 + C \cdot e^{\frac{-E_a}{k_B T_1}}}{1 + C \cdot e^{\frac{-E_a}{k_B T_2}}}$$

Throughout this work, $T_1 = 300\,\mathrm{K}$ and $T_2 = 500\,\mathrm{K}$. The thermal quenching rate is simply given by:

$$\mathrm{TQ} = 1 - \mathrm{TS}$$

Assuming that the cross-over and auto-ionization mechanisms operate independently, the overall TS is then given by:

$$\mathrm{TS} = \mathrm{TS}^{co} \times \mathrm{TS}^{ai} = (1 - K\Delta\mathrm{AED}) \frac{1 + C \cdot e^{\frac{-E_a^{ai}}{k_B T_1}}}{1 + C \cdot e^{\frac{-E_a^{ai}}{k_B T_2}}}$$

where ΔAED is the change in local activator environment distribution, the assumption that TQ^{co} is a linear function of ΔAED is used and K is a fitted constant, and E_a^{ai} is the activator barrier under the Dorenbos auto-ionization model.

Therefore, the overall TQ model is given as:

$$\mathrm{TQ} = 1 - (1 - K\Delta\mathrm{AED})\frac{1 + C \cdot e^{\frac{-E_a^{ai}}{k_B T_1}}}{1 + C \cdot e^{\frac{-E_a^{ai})}{k_B T_2}}} \quad \text{(S1)}$$

where E_a^{ai} is expressed as a linear function of the host band gap, i.e., $E_a^{ai} = AE_g + B$. [14]

The values of the unknown constants K, A and B, were determined by performing a least-squares minimization of the predicted TQ from Eq. S1 with the experimentally-observed TQ of 29 phosphors (given in Table S1). This minimization was carried out using the SciPy package using the BFGS algorithm. [15]

Table SI. Structural and thermal quenching properties for 29 oxide phosphors. The TQ data presented here is experimental value collected from corresponding cited references. E_g (unit: eV) is the host band gap calculated using the PBE functional. ΔAED is the difference in the activator environment distribution (AED) between 300 K and 500 K. $Area(Y)$ is the computed Voronoi area. E_a^{ai} (unit: eV) is the predicted activation energy. Θ_D (unit: K) is DFT calculated Debye temperature using PBE functional.

Host material	Space group	Activator	TQ%	E_g	ΔAED	Area	E_a^{ai}	Θ_D	Refs.
$Lu_3Al_5O_{12}$	$Ia\bar{3}d$	Ce^{3+}	3	5.04	0.027	88.2	0.89	605.8	[16–18]
$Ba_9Lu_2Si_6O_{24}$	$R\bar{3}$	Ce^{3+}	10	4.62	0.022	86.6	0.82	398.3	[19]
$Y_3Al_5O_{12}$	$Ia\bar{3}d$	Ce^{3+}	6	4.58	0.030	78.4	0.81	712.8	[13,20,21]
$Ca_3Sc_2Si_3O_{12}$	$Ia\bar{3}d$	Ce^{3+}	7	4.10	0.017	95.0	0.74	672.6	[22–24]
$Ba_9Y_2Si_6O_{24}$	$R\bar{3}$	Ce^{3+}	15	4.51	0.016	86.0	0.81	388.3	[25]
$BaLu_2Si_3O_{10}$	$P2_1/m$	Ce^{3+}	57	4.82	0.120	14.5	0.86	406.5	[26]
$Ba_2Y_5B_5O_{17}$	$Pbcn$	Ce^{3+}	71	4.50	0.120	38.0	0.80	392.4	[27]
$Y_3Mg_2AlSi_2O_{12}$	$Ia\bar{3}d$	Ce^{3+}	80	3.94	0.100	12.0	0.71	652.0	[28]
$Gd_3Al_5O_{12}$	$Ia\bar{3}d$	Ce^{3+}	65	3.46	0.080	79.1	0.63	500.9	[29]
$Ba_3Y_2B_6O_{15}$	$Ia\bar{3}$	Ce^{3+}	82	4.52	0.140	95.0	0.81	379.0	[30]
$K_3YSi_2O_7$	$P6_3/mcm$	Ce^{3+}	99	3.67	0.140	95.0	0.66	515.2	[31]
$SrMgAl_{10}O_{17}$	$P6_3/mmc$	Eu^{2+}	12	4.80	0.043	40.0	0.91	656.9	[32,33]
$KSrPO_4$	Pm	Eu^{2+}	20	5.10	0.120	47.8	0.94	292.8	[34]
$KBaPO_4$	Pnm	Eu^{2+}	15	4.95	0.130	55.0	0.92	332.9	[35]
Sr_2LiAlO_4	$P2_1/m$	Eu^{2+}	12	4.19	0.028	67.0	0.83	467.5	[36]
$BaZrSi_3O_9$	$P\bar{6}2c$	Eu^{2+}	25	4.68	0.110	80.0	0.89	493.1	[37,38]
$BaSc_2Si_3O_{10}$	$P2_1/m$	Eu^{2+}	50	4.73	0.170	30.0	0.89	529.2	[32]
Sr_3SiO_5	$P4/ncc$	Eu^{2+}	35	3.76	0.036	82.0	0.78	402.7	[39]
$Ba_2MgSi_2O_7$	$C2/c$	Eu^{2+}	27	4.45	0.063	69.0	0.86	386.6	[40]
$SrLiPO_4$	$P6_3$	Eu^{2+}	32	4.42	0.120	41.6	0.86	378.9	[35]
Sr_2SiO_4	$Pmcm$	Eu^{2+}	63	4.38	0.160	38.0	0.85	431.7	[41]
$BaLu_2Si_3O_{10}$	$P2_1/m$	Eu^{2+}	62	4.82	0.210	23.0	0.90	406.5	[42]
$Sr_2Al_2SiO_7$	$P\bar{4}2_1m$	Eu^{2+}	50	4.20	0.110	37.0	0.83	514.6	[43–45]
Ba_2SiO_4	$Pmcm$	Eu^{2+}	60	4.63	0.220	22.3	0.89	311.3	[41]
$Ca_6BaP_4O_{17}$	$C2/m$	Eu^{2+}	82	4.26	0.190	11.0	0.84	507.8	[46]
$Ca_7Mg(SiO_4)_4$	$Pnn2$	Eu^{2+}	60	4.18	0.110	34.4	0.83	601.0	[47]
$CaMgSi_2O_6$	$Pmcm$	Eu^{2+}	75	4.55	0.200	25.0	0.88	665.0	[47]
$Sr_2MgSi_2O_7$	$P\bar{4}2_1m$	Eu^{2+}	20	4.49	0.059	68.0	0.87	475.7	[48]
$SrSc_2O_4$	$Pnma$	Eu^{2+}	80	3.44	0.160	84.0	0.74	604.7	[49]

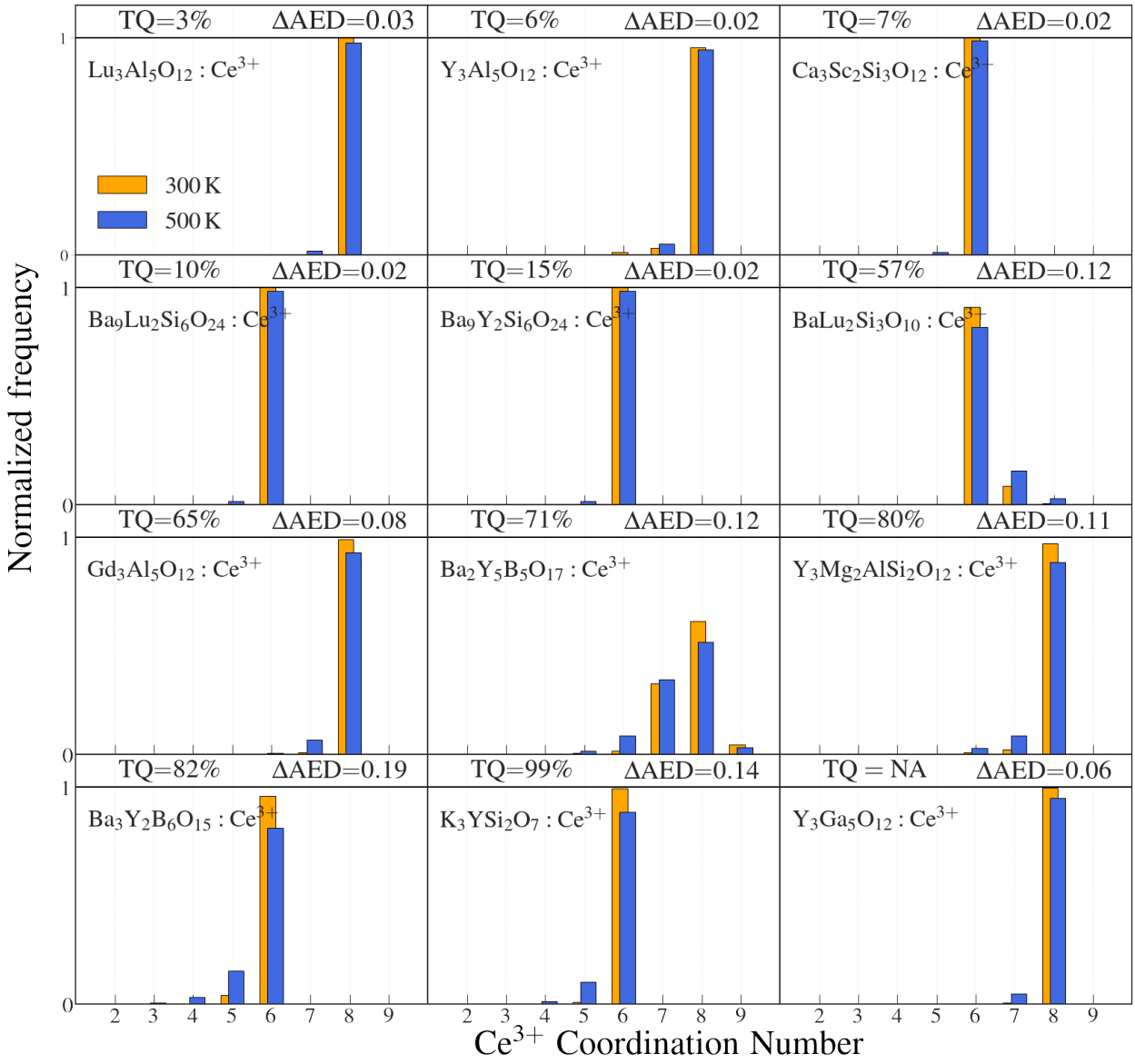

FIG. S1. The activator environment distribution for Ce^{3+}-activated hosts at 300 K and 500 K. Experimental TQ rates as well as the computed ΔAED are shown. Note, the TQ rate of $Y_3Ga_5O_{12}$:Ce^{3+} is not applicable here, as its quantum efficiency is measured to be 0 between 300 K and 500 K. The AED of $Y_3Ga_5O_{12}$:Ce^{3+} are shown for comparison purposes between other garnet structures.

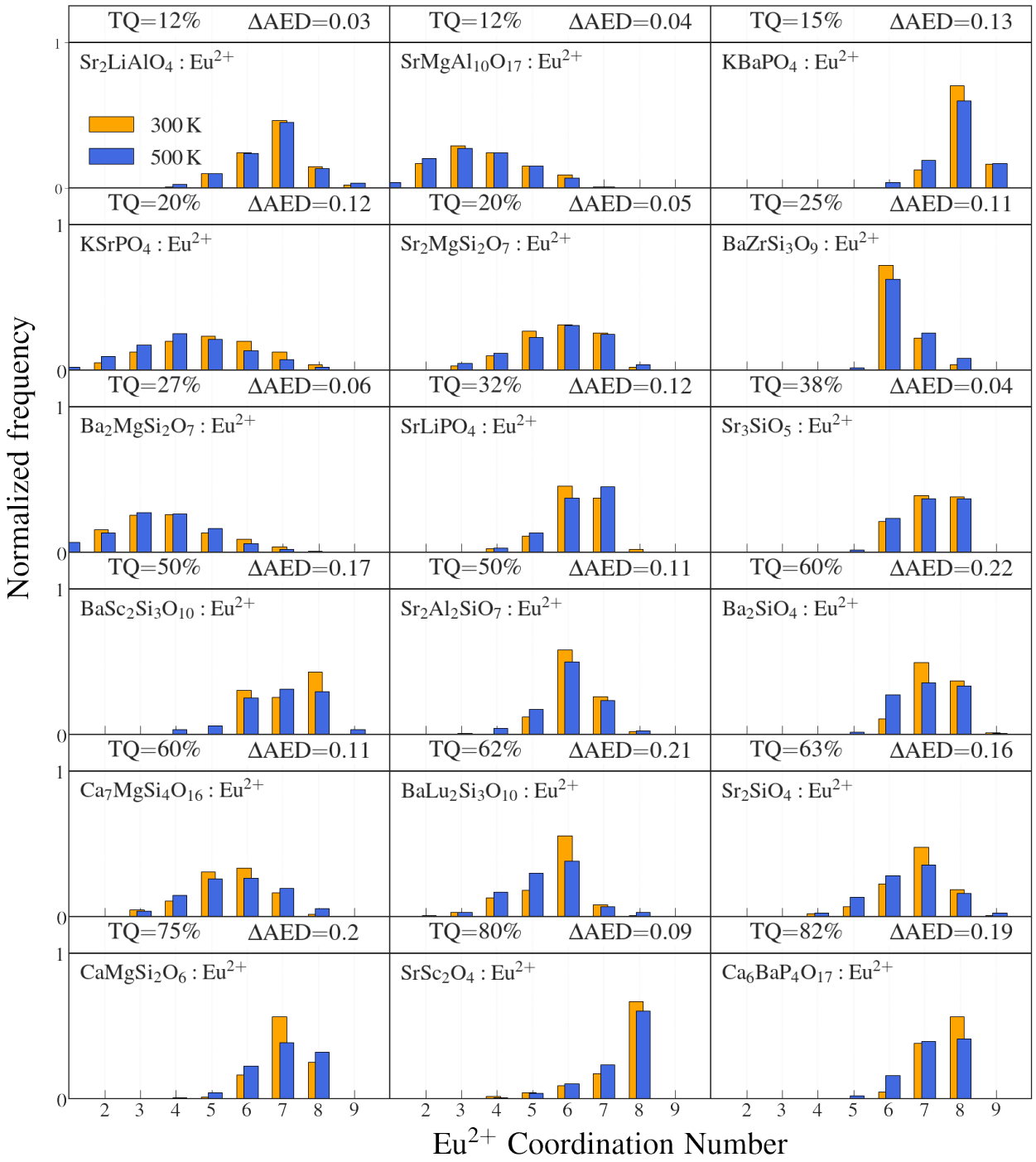

FIG. S2. The activator environment distribution for Eu^{2+}-activated hosts at 300 K and 500 K. Experimental TQ rates as well as the computed ΔAED are shown.

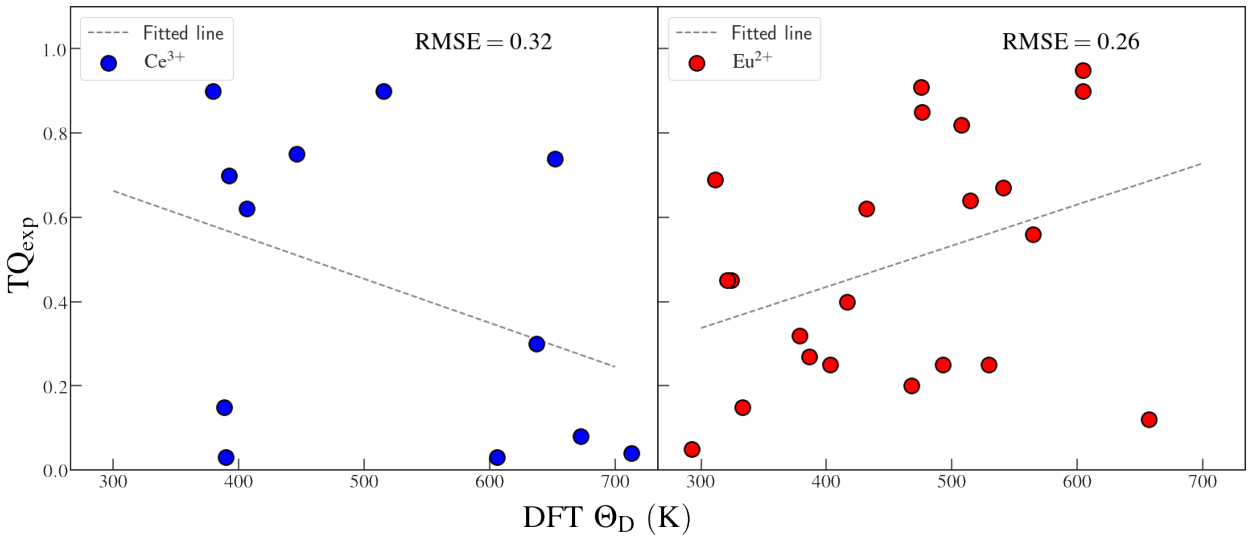

FIG. S3. TQ_{exp} against the DFT-calculated Debye temperature (Θ_D)

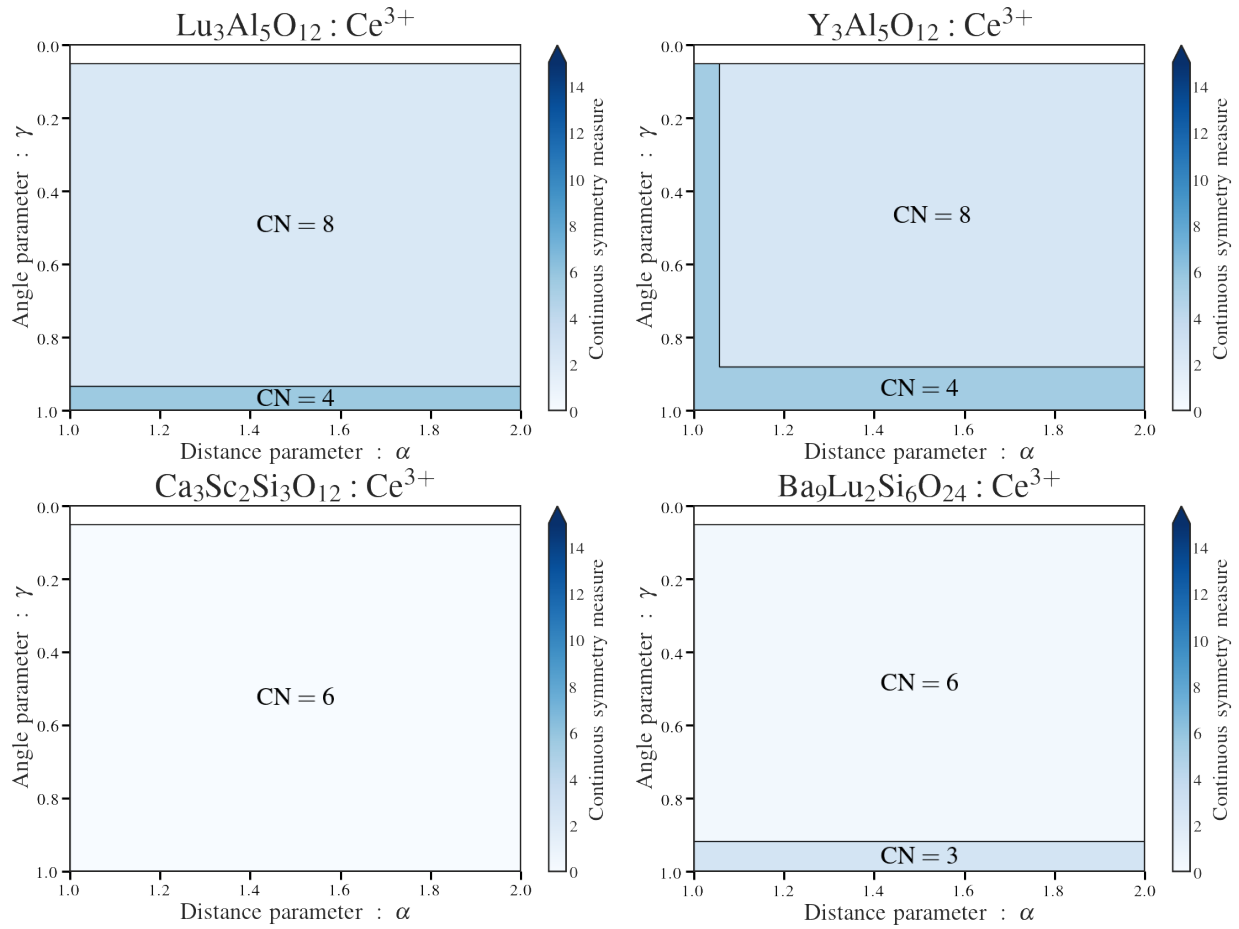

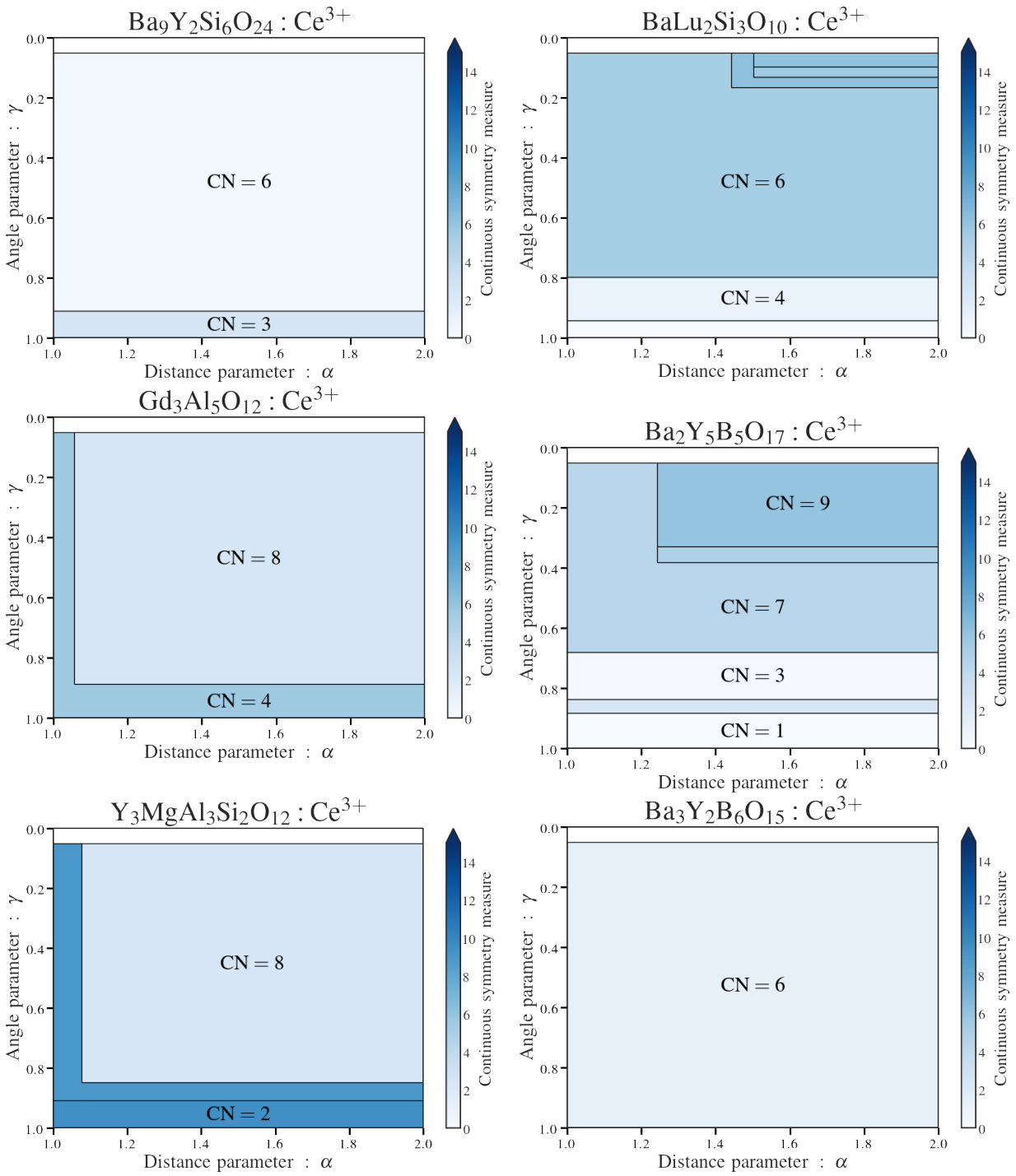
$Ba_9Y_2Si_6O_{24} : Ce^{3+}$
CN = 6
CN = 3
$BaLu_2Si_3O_{10} : Ce^{3+}$
CN = 6
CN = 4
$Gd_3Al_5O_{12} : Ce^{3+}$
CN = 8
CN = 4
$Ba_2Y_5B_5O_{17} : Ce^{3+}$
CN = 9
CN = 7
CN = 3
CN = 1
$Y_3MgAl_3Si_2O_{12} : Ce^{3+}$
CN = 8
CN = 2
$Ba_3Y_2B_6O_{15} : Ce^{3+}$
CN = 6
Angle parameter : γ
Distance parameter : α
Continuous symmetry measure

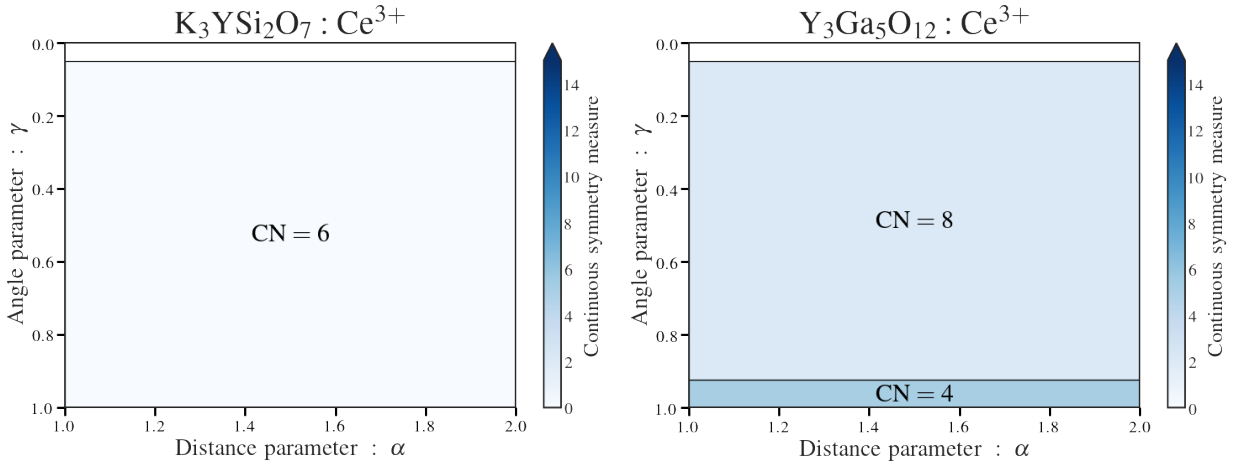

FIG. S4. The Voronoi grid representation of Ce^{3+} local environment of all Ce^{3+}-activated hosts in Table S1. The coordination number (CN) in red reflects the environment considered to compute the Voronoi area.

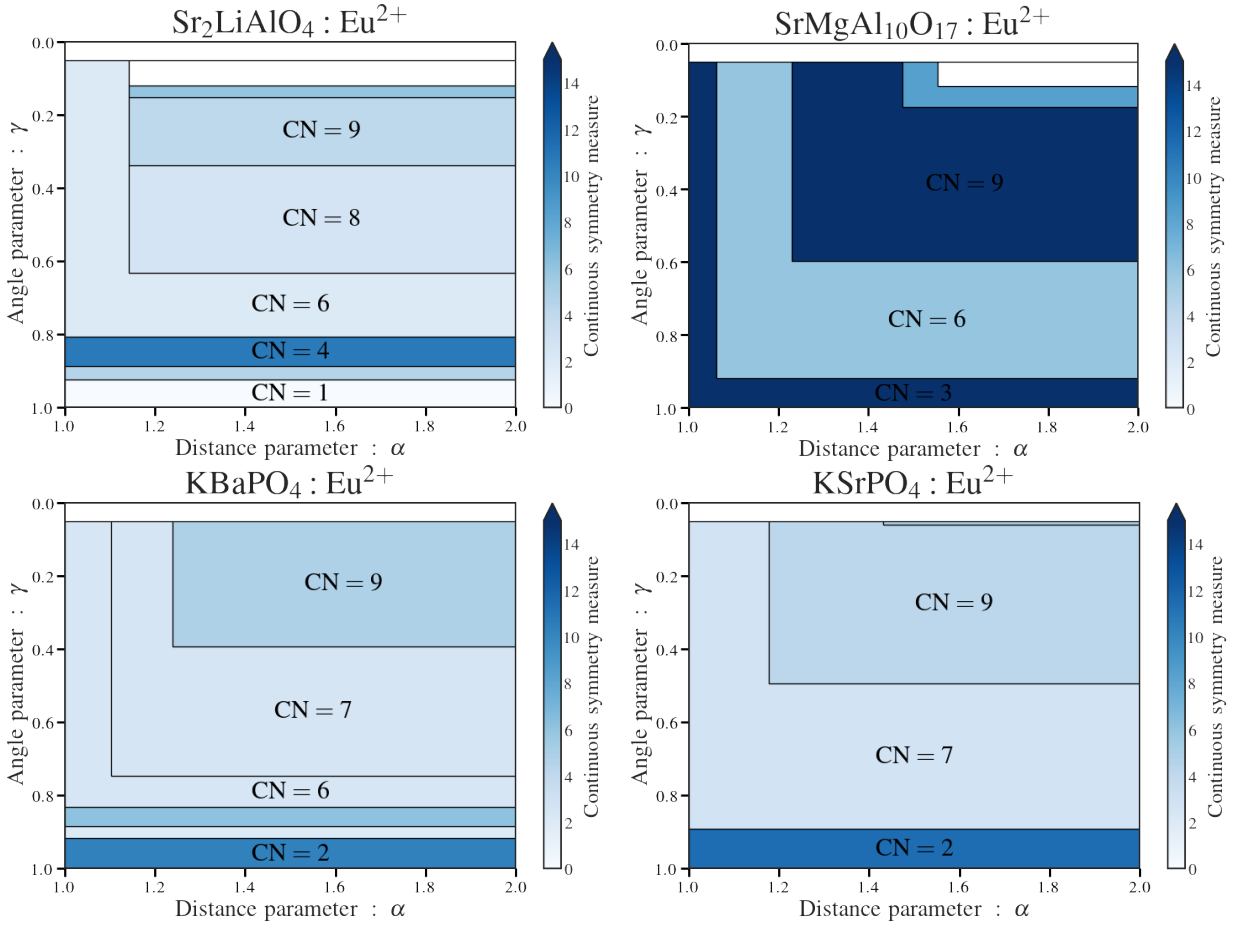

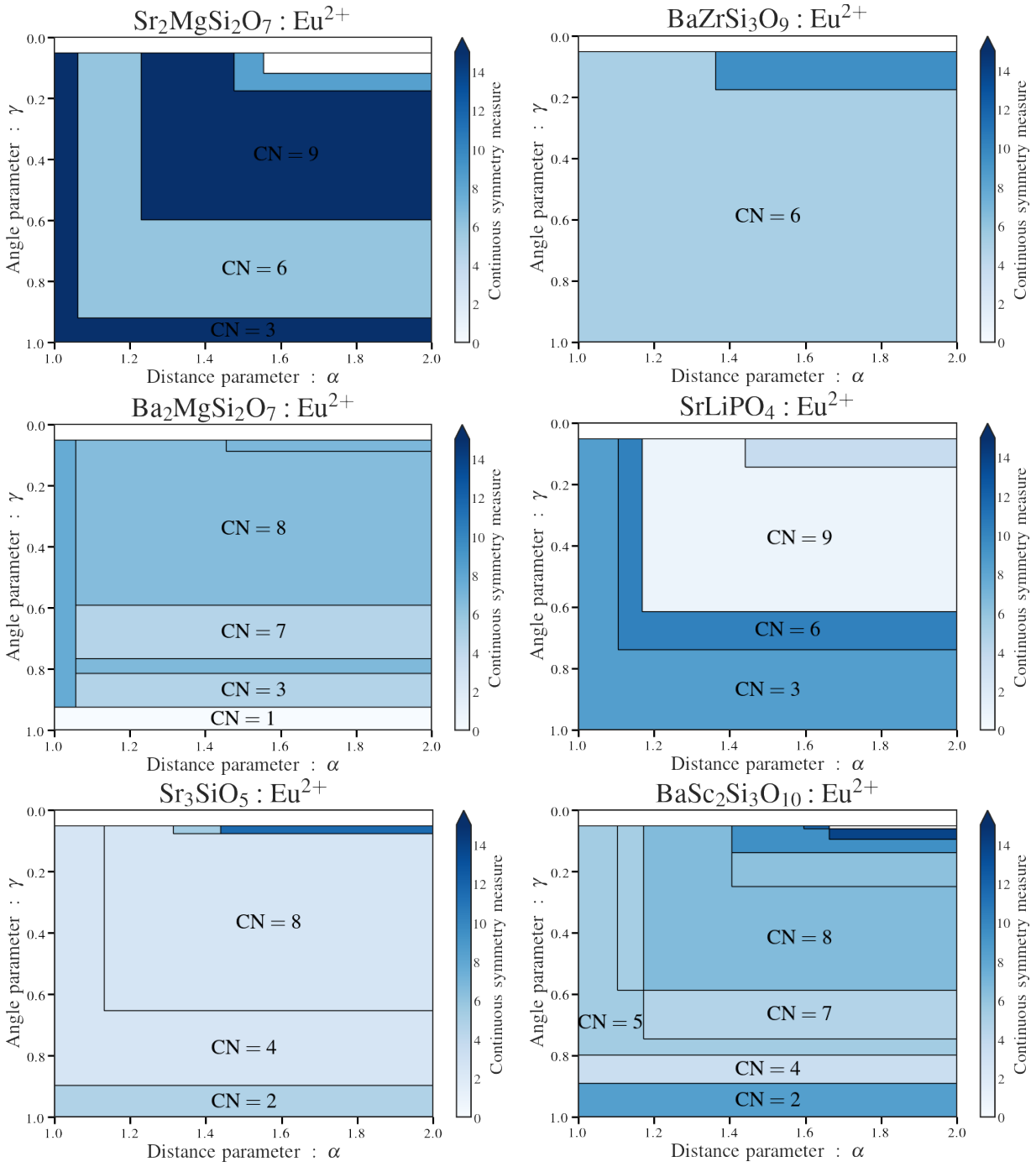
$Sr_2MgSi_2O_7 : Eu^{2+}$
CN = 9
CN = 6
CN = 3
$BaZrSi_3O_9 : Eu^{2+}$
CN = 6
$Ba_2MgSi_2O_7 : Eu^{2+}$
CN = 8
CN = 7
CN = 3
CN = 1
$SrLiPO_4 : Eu^{2+}$
CN = 9
CN = 6
CN = 3
$Sr_3SiO_5 : Eu^{2+}$
CN = 8
CN = 4
CN = 2
$BaSc_2Si_3O_{10} : Eu^{2+}$
CN = 8
CN = 7
CN = 5
CN = 4
CN = 2
Angle parameter : γ
Distance parameter : α
Continuous symmetry measure

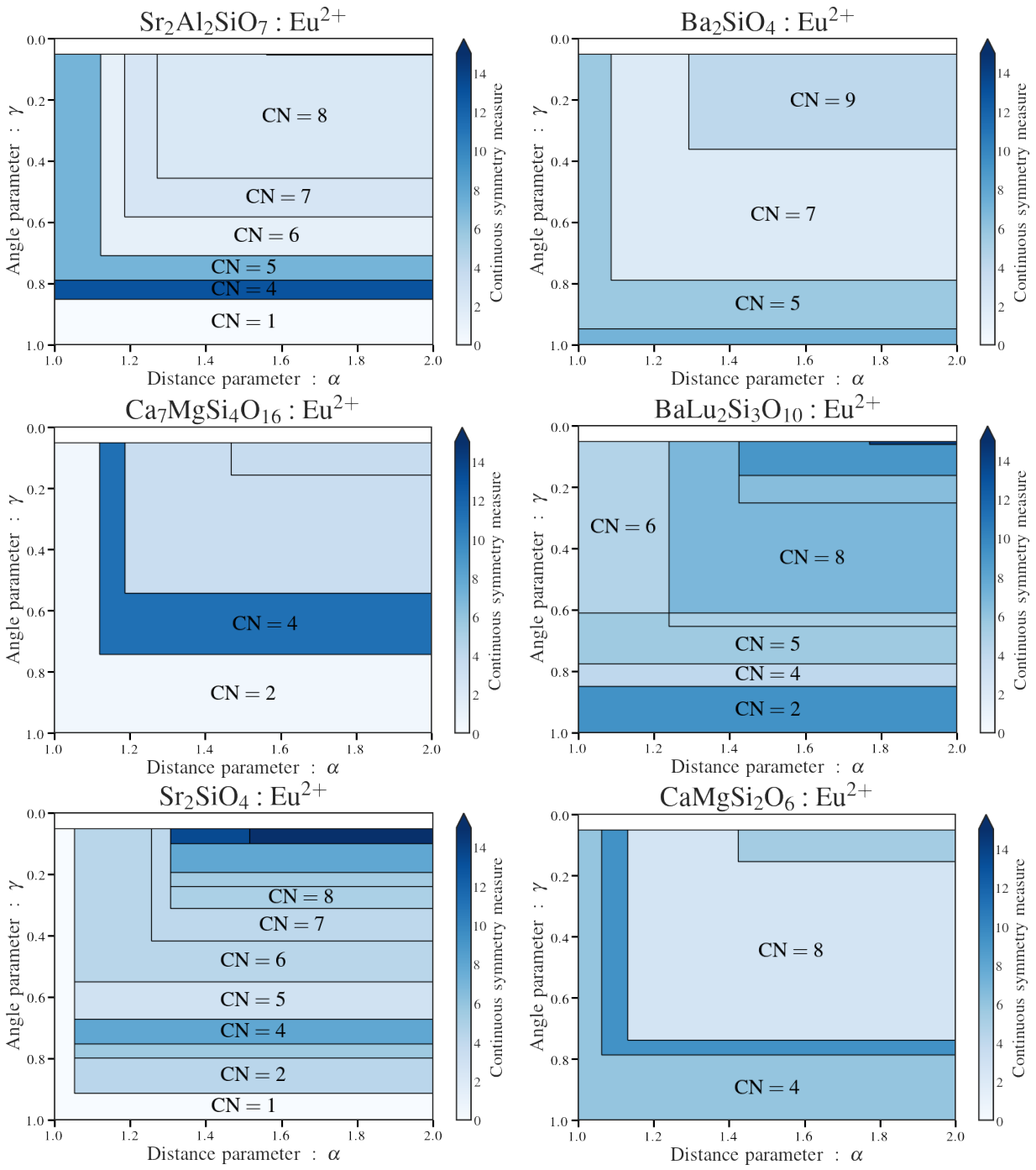
$Sr_2Al_2SiO_7 : Eu^{2+}$
CN = 8
CN = 7
CN = 6
CN = 5
CN = 4
CN = 1
$Ba_2SiO_4 : Eu^{2+}$
CN = 9
CN = 7
CN = 5
$Ca_7MgSi_4O_{16} : Eu^{2+}$
CN = 4
CN = 2
$BaLu_2Si_3O_{10} : Eu^{2+}$
CN = 6
CN = 8
CN = 5
CN = 4
CN = 2
$Sr_2SiO_4 : Eu^{2+}$
CN = 8
CN = 7
CN = 6
CN = 5
CN = 4
CN = 2
CN = 1
$CaMgSi_2O_6 : Eu^{2+}$
CN = 8
CN = 4
Angle parameter : γ
Distance parameter : α
Continuous symmetry measure

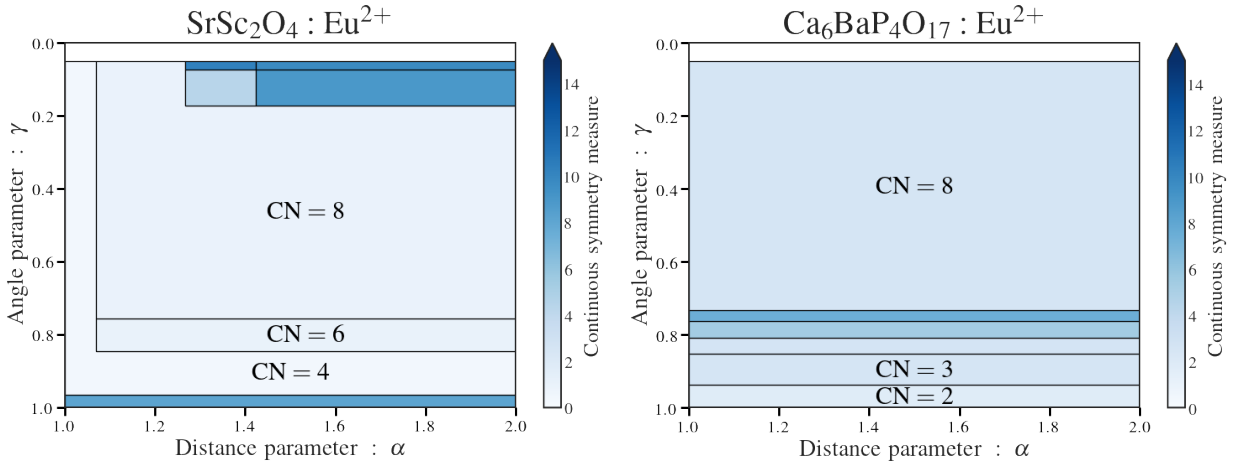

FIG. S5. The Voronoi grid representation of Eu^{2+} local environment of all Eu^{2+}-activated hosts in Table S1.

References

[1] G. Kresse and J. Furthmüller, Physical Review B **54**, 11169 (1996).
[2] P. E. Blöchl, Phys. Rev. B **50**, 17953 (1994).
[3] J. P. Perdew, K. Burke, and M. Ernzerhof, Physical Review Letters **77**, 3865 (1996).
[4] S. P. Ong, S. Cholia, A. Jain, M. Brafman, D. Gunter, G. Ceder, and K. A. Persson, Computational Materials Science **97**, 209 (2015).
[5] A. Chaudhry, R. Boutchko, S. Chourou, G. Zhang, N. Grønbech-Jensen, and A. Canning, Phys. Rev. B **89**, 155105 (2014).
[6] S. P. Ong, W. D. Richards, A. Jain, G. Hautier, M. Kocher, S. Cholia, D. Gunter, V. L. Chevrier, K. A. Persson, and G. Ceder, Computational Materials Science **68**, 314 (2013).
[7] W. G. Hoover, **31**, 1695 (1985).
[8] J. Brgoch, S. P. DenBaars, and R. Seshadri, The Journal of Physical Chemistry C **117**, 17955 (2013).
[9] D. Waroquiers, X. Gonze, G. M. Rignanese, C. Welker-Nieuwoudt, F. Rosowski, M. Göbel, S. Schenk, P. Degelmann, R. André, R. Glaum, and G. Hautier, Chemistry of Materials **29**, 8346 (2017).
[10] R. Hoppe, **9**, 25 (1970).
[11] C. R. Ronda, Emission and Excitation Mechanisms of Phosphors (2007).
[12] P. Dorenbos, Journal of Physics: Condensed Matter **17**, 8103 (2005).
[13] J. Ueda, P. Dorenbos, A. J. J. Bos, A. Meijerink, and S. Tanabe, The Journal of Physical Chemistry C **119**, 25003 (2015).
[14] Z. Wang, I.-H. Chu, F. Zhou, and S. P. Ong, Chemistry of Materials **28**, 4024 (2016).
[15] Jones E, Oliphant E, Peterson P, SciPy: Open Source Scientific Tools for Python (2001).
[16] K. Park, T. Kim, Y. Yu, K. Seo, and J. Kim, Journal of Luminescence **173**, 159 (2016).
[17] J. Xu, W. Chen, R. Zeng, and D. Peng, Materials Letters **133**, 1 (2014).
[18] Y.-H. Song, E.-J. Chung, M.-K. Jung, T. Masaki, K. Senthil, S.-J. Lee, J.-S. Yoo, and D.-H. Yoon, Materials Letters **116**, 337 (2014).
[19] Y. Liu, J. Silver, R.-J. Xie, J. Zhang, H. Xu, H. Shao, J. Jiang, and H. Jiang, Journal of Materials Chemistry C **5**, 12365 (2017).
[20] V. M. Bachmann, **126**, 87 (2009).
[21] L. Chen, C. C. Lin, C. W. Yeh, and R. S. Liu, Materials **3**, 2172 (2010).
[22] T. Akai, M. Shigeiwa, K. Okamoto, Y. Shimomura, N. Kijima, and T. Honma, AIP Conference Proceedings **882**, 389 (2007).
[23] Y. Shimomura, T. Honma, M. Shigeiwa, T. Akai, K. Okamoto, and N. Kijima, Journal of The Electrochemical Society **154**, J35 (2007).
[24] C. J. B. I. Levchuk, F. Schröppel, L. Römling, A. Osvet, N. Khaidukov, Y. Zorenko, R. Van Deun, M. Batentschuk, Photonic Materials & Devices 194 (2017).
[25] J. Brgoch, C. K. H. Borg, K. A. Denault, A. Mikhailovsky, S. P. Denbaars, and R. Seshadri, Inorganic Chemistry **52**, 8010 (2013).
[26] K. Li, S. Liang, H. Lian, M. Shang, B. Xing, and J. Lin, Journal of Materials Chemistry C **4**, 3443 (2016).
[27] M. Hermus, P.-C. Phan, and J. Brgoch, Chem. Mater. **28**, 1121 (2016).
[28] A. Katelnikovas, H. Bettentrup, D. Uhlich, S. Sakirzanovas, T. Jüstel, and A. Kareiva, Journal of Luminescence **129**, 1356 (2009).

[29] J. M. Ogiegło, A. Zych, K. V. Ivanovskikh, T. Jüstel, C. R. Ronda, and A. Meijerink, The Journal of Physical Chemistry A **116**, 8464 (2012).
[30] A. C. Duke, S. Hariyani, and J. Brgoch, Chem. Mater. **30**, 2668 (2018).
[31] J. Qiao, M. Amachraa, M. Molokeev, Y.-C. Chuang, S. P. Ong, Q. Zhang, and Z. Xia, Chem. Mater. (2019).
[32] H. Onuma, S. I. D. Student, and C. A. Del Carpio, 211 (2010).
[33] L. Wang, H. Zhang, Y. Li, P. Liang, Y. Shen, and F. Jiao, International Journal of Applied Ceramic Technology **13**, 185 (2016).
[34] Y. S. Tang, S. F. Hu, C. C. Lin, N. C. Bagkar, and R. S. Liu, Applied Physics Letters **90**, 4 (2007).
[35] C. C. Lin, Z. R. Xiao, G.-Y. Guo, T.-S. Chan, and R.-S. Liu, Journal of the American Chemical Society **132**, 3020 (2010).
[36] Z. Wang, J. Ha, Y. H. Kim, W. B. Im, J. McKittrick, and S. P. Ong, Joule **2**, 914 (2018).
[37] D. Y. Wang, C. H. Huang, Y. C. Wu, and T. M. Chen, Journal of Materials Chemistry **21**, 10818 (2011).
[38] T. Komukai, Y. Takatsuka, H. Kato, and M. Kakihana, Journal of Luminescence **158**, 328 (2015).
[39] E.-H. Kang, S.-W. Choi, S. E. Chung, J. Jang, S. Kwon, and S.-H. Hong, Journal of The Electrochemical Society **158**, J330 (2011).
[40] X. Zhang, J. Zhang, R. Wang, and M. Gong, Journal of the American Ceramic Society **93**, 1368 (2010).
[41] J. S. Kim, Y. H. Park, S. M. Kim, J. C. Choi, and H. L. Park, Solid State Communications **133**, 445 (2005).
[42] J. Brgoch, K. Hasz, K. A. Denault, C. K. H. Borg, A. A. Mikhailovsky, and R. Seshadri, Faraday Discussions **176**, 333 (2014).
[43] Y. Q. Li, N. Hirosaki, R. J. Xie, and M. Mitomo, Science and Technology of Advanced Materials **8**, 607 (2007).
[44] F.-C. Lu, L.-J. Bai, W. Dang, Z.-P. Yang, and P. Lin, ECS Journal of Solid State Science and Technology **4**, R27 (2014).
[45] W. Zhou, X. Ma, M. Zhang, Y. Luo, and Z. Xia, Journal of Rare Earths **33**, 700 (2015).
[46] N. Komuro, M. Mikami, Y. Shimomura, E. G. Bithell, and A. K. Cheetham, Journal of Materials Chemistry C **3**, 204 (2015).
[47] J. Ha, Z. Wang, E. Novitskaya, G. A. Hirata, O. A. Graeve, S. P. Ong, and J. McKittrick, Journal of Luminescence **179**, 297 (2016).
[48] X. Zhang, X. Tang, J. Zhang, H. Wang, J. Shi, and M. Gong, Powder Technology **204**, 263 (2010).
[49] M. Müller, M. F. Volhard, and T. Jüstel, RSC Advances **6**, 8483 (2016).